International Journal of Multiphase Flow 171 (2024) 104689

Contents lists available at ScienceDirect

International Journal of Multiphase Flow

journal homepage: www.elsevier.com/locate/ijmulflow

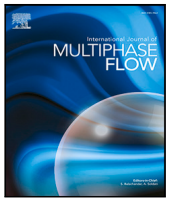

Scaling analysis of thermal bubble-driven micro-pumps from micro-scale to meso-scale

Brandon Hayes, Kaushik Jayaram, Robert MacCurdy *

University of Colorado Boulder, Paul M. Rady Department of Mechanical Engineering, Boulder, CO, 80309, USA

ARTICLE INFO

Keywords:
Microfluidics
Mesofluidics
Phase change
Inertial pumping
Scaling analysis

ABSTRACT

Thermal bubble-driven micro-pumps are an upcoming micro-actuator technology that can be directly integrated into micro/mesofluidic channels, have no moving parts, and leverage existing mass production fabrication approaches. As such, these micro-pumps hold great promise for micro/mesofluidic systems such as lab-on-a-chip technologies. To date, thermal bubble-driven micro-pumps have been realized discretely at the micro-scale (10's of μm) and meso-scale (100's of μm) which result in flow rates on the order of pL/pulse to nL/pulse respectively. However, no current work has studied how pump performance scales as a function of pump area. In this study, a systematic scaling analysis from micro to meso-scale (10-1000 μm) of thermal bubble-driven micro-pumps is performed to develop reduced parameter one-dimensional (1D) models with pump area dependency. We present, for the first time, an empirical relationship between bubble strength and resistor area across 4 orders of magnitude that generalizes the prevailing reduced parameter 1D model. Namely, $q_o(A) = (1.253 \times 10^{-12})A\ [kg \cdot m/s]$ which was found to fit the data with an R^2 value of 0.96. Previously, experimental data were required to estimate the bubble strength of a particular micro/mesofluidic channel with a thermal bubble-driven micro-pump of a given area. In this work, the developed empirical relationship estimates bubble strength as a function of resistor area thus eliminating the need for experimental data to perform a first-order analysis of thermal bubble-driven micro-pumps. We envision such reduced parameter 1D models as an important first-order design tool for micro/mesofluidic designers to predict the size of the pump area needed for a desired flow rate.

1. Introduction

At its core, design of micro/mesofluidic devices consists of assemblies of channels and actuators to perform fluidic operations. The channel geometry and type of actuator is tailored to meet a specific application. For instance, fluid may need to be routed at high flow rates (Zhou et al., 2018), be pulsatile (Mutlu et al., 2018), or be precisely dispensed (Davies et al., 2020). As such, the choice of fluidic actuator is critical to the function of a micro/mesofluidic system. Modern micro-pumps have utilized a variety of physics to move fluid at the micro/nano scale such as electrostatic (Mishchuk et al., 2009; Snyder et al., 2013), magnetic (Shizhi and Bau, 2009), centrifugal (Duffy et al., 1999), peristaltic (Vinayakumar et al., 2017), piezoelectric (Ma et al., 2019), capillary action (Hassan and Zhang, 2020), thermal gradients (Lotfian and Roohi, 2019), and mechanical pressure (Lake et al., 2017). Thermal bubble-driven micro-pumps (also known as inertial micro-pumps) are an upcoming actuation technology for moving fluid without the use of external pump sources or moving parts and can be directly integrated into micro/mesofluidic channels using existing mass fabrication infrastructure (Torniainen et al., 2012; Govyadinov et al., 2016). Thus, these micro-pumps hold great potential for enabling commercial "lab-on-a-chip" technologies. However, to date, thermal bubble-driven micro-pumps have only been discretely demonstrated at the micro-scale (10's μm) and meso-scale (100's of μm) (Govyadinov et al., 2016; Kornilovitch et al., 2022; Hayes et al., 2022). Little is known about how the pump dynamics and flow rate change as a function of micro-pump size. In a realistic micro/mesofluidic application, the size of the micro-pump along with channel size will be tailored to the desired flow rate in a channel; as such, understanding how these micro-pumps scale is critical to commercial applications of this technology.

Thermal bubble-driven micro-pumps were first theorized and demonstrated by Yuan and Prosperetti (1999), Ory et al. (2000) and Yin and Prosperetti (2005) in the 2000's and commercialized by Hewlett–Packard Inc., Torniainen et al. (2012), around 2010. Based on thermal inkjet (TIJ) technology, these micro-pumps consist of a micro-resistor that locally boils liquid in a micro-channel generating a

* Corresponding author.
E-mail address: maccurdy@colorado.edu (R. MacCurdy).

https://doi.org/10.1016/j.ijmultiphaseflow.2023.104689
Received 11 September 2023; Received in revised form 13 November 2023; Accepted 27 November 2023
Available online 5 December 2023

vapor bubble which performs mechanical work. A voltage pulse lasting a few microseconds superheats an interfacial layer of fluid above the resistor's surface close to its critical point (approximately 300 °C for water) which causes explosive boiling (Einat and Grajower, 2010). The high pressure vapor bubble rapidly expands in the channel until its internal pressure falls below ambient pressure upon which the bubble collapses (Govyadinov et al., 2016). Since the vapor bubble forms in a subcooled liquid, after bubble collapse, the vapor bubble re-dissolves back into the fluid (Einat and Grajower, 2010). When placed asymmetrically in a micro-channel with reservoirs at either end, the momentum imbalance upon bubble collapse creates a net fluid pumping effect for each actuation pulse (Kornilovitch et al., 2022, 2013).

In an arbitrary micro/mesofluidic system, a range of flow rates and flow control are often needed. For instance, consider a microfluidic oil–water droplet generator. The size of the droplets and droplet spacing are controlled primarily by the ratio of flow rates in the feed channels (Ibrahim et al., 2021). As such, thermal bubble-driven micro-pumps must be able to operate over a range of flow rates and flow control. There are two primary control mechanisms to vary the flow rate of these micro-pumps: (1) firing frequency and (2) resistor size. The effect of firing frequency on thermal bubble-driven micro-pumps has been well studied at the micro-scale in which the flow rate increases proportionally with firing frequency up to the limit when fluid no longer is at rest at the start of the next firing event (Torniainen et al., 2012; Govyadinov et al., 2016). However, to date, thermal bubble-driven micro-pumps have been solely studied at discrete resistor sizes on the micro-scale ($15 \times 33.3\ \mu m^2$) and meso-scale ($300 \times 700\ \mu m^2$). No work has described how the bubble dynamics and flow physics change from micro to meso-scale. Thus, the present work studies how thermal bubble-driven micro-pump bubble and flow physics vary as a function of micro-pump size. In this work, we investigate micro-pump scaling from the micro-scale to meso-scale and develop reduced parameter one-dimensional (1D) models to account for pump size. To our knowledge, this is the first work that investigates thermal bubble-driven micro-pump size scaling and describes the empirical relationship between bubble strength and resistor area in an attempt to make the reduced parameter 1D model (see Govyadinov et al., 2016; Kornilovitch et al., 2013 for a complete derivation) of thermal bubble-driven micro-pumps more generalized. Instead of requiring experimental data to estimate the bubble strength for a particular microfluidic channel with a thermal bubble-driven micro-pump of a given area, this work provides an estimate for the bubble strength as a function of the resistor area using the reduced parameter 1D model thus eliminating the need for experimental data to perform a first-order analysis of thermal bubble-driven micro-pumps. Additionally, we demonstrate that these micro-pumps can produce flow rates ranging from pL/pulse ($15 \times 33.3\ \mu m^2$ resistors) to nL/pulse ($500 \times 1000\ \mu m^2$ resistors) with a maximum theoretical firing frequency ranging from 10's of kHz to 100's of Hz respectively. We envision that a realistic micro/mesofluidic system using thermal bubble-driven micro-pumps will incorporate a variety of micro-pump sizes ranging from smaller micro-pumps to enable high precision fluid handling to larger micro-pumps to enable high throughput, high flow rate fluid handling. As such, this work provides a foundation to estimate the size of the micro-pump needed to achieve a desired flow rate for microfluidic designers.

2. Pump physics

2.1. Operating principle

Although geometrically simple, the physics underlying the operation of thermal bubble-driven micro-pumps are complex. During a microsecond heating pulse, fluid is heated to near its critical temperature (300 °C for water) at heating rates of 100 °C/μs (Einat and Grajower, 2010). This thermal impulse results in explosive boiling at the resistor's surface which forms a single high pressure vapor bubble (Okuyama et al., 2006). If the resistor is placed asymmetrically in a channel between two reservoirs, the expansion–collapse dynamics of the vapor bubble result in unidirectional flow from the short to the long leg of the channel (Govyadinov et al., 2016), where "short leg" refers to the shorter channel segment from the reservoir to the center of the resistor as shown in Fig. 1. A detailed discussion of the pump physics can be found in our past work (Hayes et al., 2021) which is summarized below for completeness.

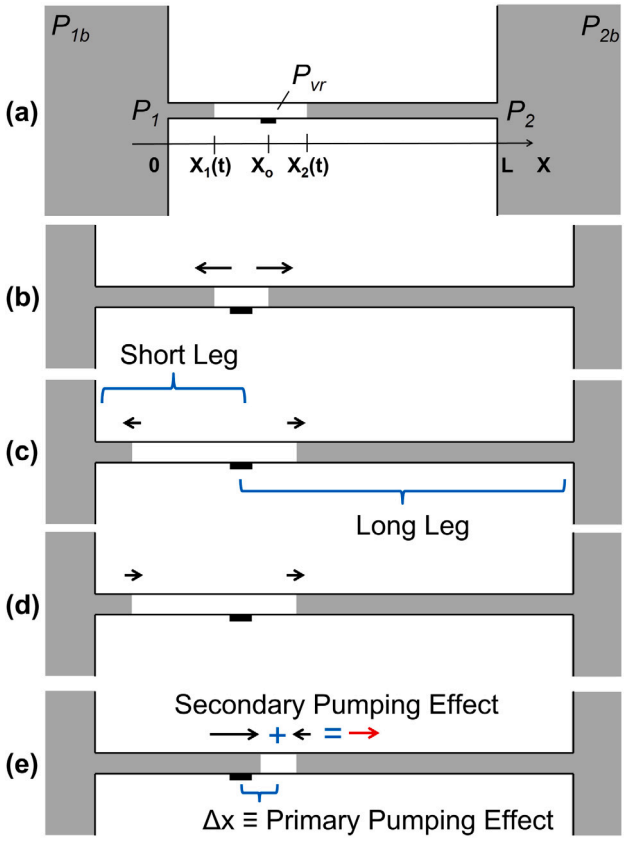

Fig. 1. Pump dynamics — illustrates the pumping process for a thermal bubble-driven micro-pump. (a) depicts the one-dimensional (1D) model setup for a micro-resistor placed at $x = x_o$ between two reservoirs in a channel of length L. During a heating pulse, fluid is locally boiled above the resistor's surface creating a high pressure vapor bubble (b) that then expands in the channel displacing fluid (c). Fluid has less mass in the short leg than the long leg which results in the short bubble leg having a greater acceleration. As the vapor bubble expands, it loses energy until its internal pressure drops below atmospheric pressure upon which the vapor bubble collapses (d). The point of complete bubble collapse occurs a distance Δx from the resistor center which represents the *primary pumping effect*, and the momentum of the short leg upon collapse is greater than that of the long leg which causes flow in the direction from short to long leg and is known as the *secondary pumping effect*. Images modified from Kornilovitch et al. "One-dimensional model of inertial pumping", *Physical Review E*, **87**, 2, 2013; used with permission from American Physical Society (Kornilovitch et al., 2013).

Consider a single vapor bubble expansion–collapse event, Fig. 1. Initially, a micro-resistor is placed at $x = x_o$ in a rectangular channel of length L between two reservoirs. A heating voltage pulse is applied to the micro-resistor which causes explosive boiling that forms a single high pressure vapor bubble, Fig. 1b. Since the short leg of the channel has less fluid and therefore less mass than the long leg, the vapor bubble accelerates faster in the direction of the short leg, Fig. 1c. As the vapor bubble expands, it loses energy resulting in a rapid pressure drop bringing the bubble pressure to sub-atmospheric pressures which causes the vapor bubble to collapse, Fig. 1d. Since momentum is dissipated faster in the short leg than the long leg due to inertia, the short bubble leg collapses faster than the long bubble leg. Thus, the vapor bubble

fully collapses at a point slightly further from the resistor center, $x = x_o + \Delta x$, and the short leg has a greater momentum than the long leg upon collapse which accelerates the fluid from the short to long leg of the channel until brought to rest by viscosity, Fig. 1e. These two effects, namely the vapor bubble collapsing at a point slightly further from the resistor center and the momentum imbalance upon collapse, result in net fluid displacement during each pump cycle and are known as the *primary pumping effect* and *secondary pumping effect* respectively (Kornilovitch et al., 2013).

2.2. Modeling of thermal bubble-driven micro-pumps

Modeling of thermal bubble-driven micro-pumps is important for fundamental understanding as well as application of these micro-pumps in commercial micro/mesofluidic systems. There are two common modeling approaches: full three-dimensional (3D) computational fluid dynamics (CFD) models (Hayes et al., 2021; Ruiz, 2007; Tan et al., 2015; Hayes et al., 2023) and reduced parameter one-dimensional (1D) models (Torniainen et al., 2012; Govyadinov et al., 2016; Kornilovitch et al., 2022; Yuan and Prosperetti, 1999; Kornilovitch et al., 2013). In 3D CFD models, thermal bubble nucleation, heat transfer, and 2-phase flow are represented mathematically as a complex system of coupled multiphysics equations. The Navier–Stokes equations describe the transport of mass, momentum, and energy for an incompressible fluid:

$$\nabla \cdot \mathbf{V} = 0 \tag{1}$$

$$\rho \frac{D\mathbf{V}}{Dt} = -\nabla P + \mu \nabla^2 \mathbf{V} + \rho \mathbf{F} \tag{2}$$

$$\rho c_p \frac{DT}{Dt} = k \nabla^2 T + q'''_{gen} \tag{3}$$

where $\mathbf{V}$ is the velocity field, ρ is the fluid density, P is the scalar pressure field, μ is the fluid viscosity, $\mathbf{F}$ is an external body force, c_p is the heat capacity at constant pressure, k is the thermal conductivity, T is the temperature, and q'''_{gen} is the volumetric heat generation. In our past work (Hayes et al., 2021), FLOW-3D was used to numerically solve the Navier–Stokes equations via the volume-of-fluid (VOF) method (Hirt and Nichols, 1981) and homogeneous bubble nucleation was modeled by approximating the vapor pressure inside the bubble as a function of bubble temperature through the Clausius–Clapeyron equation (Borgnakke and Sonntag, 1999).

Although full multiphysics 3D CFD models accurately predict bubble and flow physics, such models are computationally expensive and ill-suited for optimization or first-order microfluidic designs (Hayes et al., 2021; Ruiz, 2007). As such, reduced parameter one-dimensional (1D) models are used to rapidly design, analyze, and optimize meso/microfluidic systems with thermal bubble-driven micro-pumps. Reduced parameter 1D models simplify the complex multiphysics to tracking the evolution of fluid–vapor interfaces over time subjected to pressure initial conditions. In this study, we follow the approach from Kornilovitch et al. in which explosive boiling at the resistor's surface is described by a high pressure vapor bubble of pressure p_v, Fig. 1b, that pushes fluid out of the channel creating fluid–vapor interfaces x_1 and x_2 (Kornilovitch et al., 2013). p_v is modeled as

$$p_v(t) = \frac{q_o}{A}\delta(t) + p_{vr} \tag{4}$$

where q_o is the mechanical momentum imparted to both fluid columns denoted as the bubble strength (on the order of 10^{-10} kg m/s for a 22 $\times$ 17 μm^2 rectangular cross-section), A is the cross-section channel area, $\delta(t)$ is the Dirac delta function, and p_{vr} is the vapor saturation pressure at room temperature ($p_{vr} \approx 0.3 p_o$) (Kornilovitch et al., 2013). Once the bubble strength for a given resistor area is known, the 1D model can be used to predict bubble dynamics and flow rate; as such, the focus of this paper is determining an empirical relationship for q_o as a function of resistor area. The equations of motion for the bubble and fluid are determined by analyzing the momentum gained/lost during a bubble expansion and collapse cycle. Namely,

$$A\rho x_1 \ddot{x}_1 + \kappa x_1 \dot{x}_1 = (p_1 - p_v)A \tag{5}$$

$$A\rho(L - x_2)\ddot{x}_2 + \kappa(L - x_2)\dot{x}_2 = (p_v - p_2)A \tag{6}$$

where A is the cross-sectional channel area, ρ is the fluid density, κ is the characteristic strength of the viscous force derived in Appendix A (approximately 0.0184 Pa s for a 17 $\times$ 22 μm^2 rectangular channel cross-section), L is the channel length, p_1 and p_2 are the pressures at the channel inlet/outlet, and p_v is the bubble pressure. Pressures immediately outside the channel $p_{1,2}$ can vary from the bulk reservoir pressures $p_{1b,2b}$ due to source flow from the reservoir and is accounted for by a Bernoulli term added to the bulk reservoir pressure shown below. m = {0, 1} is a discrete parameter to select between pressure models and H(x) is the Heaviside function (Ory et al., 2000; Kornilovitch et al., 2013). We follow the approach by Kornilovitch et al. and take m = 1 to account for source flow.

$$p_1 = p_{1b} - \frac{m}{2}\rho \dot{x}_1{}^2 H(\dot{x}_1) \tag{7}$$

$$p_2 = p_{2b} - \frac{m}{2}\rho \dot{x}_2{}^2 H(-\dot{x}_2) \tag{8}$$

In a simple one bubble and one channel network, initial positions start at the resistor center and initial velocities are found through momentum balances.

Short Arm	*Long Arm*
$x_1(0) = x_o$	$x_2(0) = x_o$
$\dot{x}_1(0) = -\frac{q_o}{\rho A x_o}$	$\dot{x}_2(0) = \frac{q_o}{\rho A(L - x_o)}$

(9)

Eqs. (5)–(6) describe the bubble and flow dynamics during *pre-collapse*, where the vapor bubble expands and collapses in the channel but does not re-dissolve back into the fluid. During *post-collapse*, where the vapor bubble re-dissolved back into the fluid, the equations of motion are modified. At the time of collapse, t = t_c, the bubble is at position $x = x_c$ with short and long arm velocities $v_{(1,2)c}$. Here, we use the notation $v_{(1,2)c}$ to refer to the velocity of interface 1 and 2 respectively at the time of collapse. The end pre-collapse positions and velocities define the starting initial conditions of the post-collapse phase. As such, after complete bubble collapse, the dynamic equations become

$$A\rho L\ddot{x} + \kappa L\dot{x} = (p_1 - p_2)A \tag{10}$$

where a single interface x now models the fluid motion. From conservation of momentum, the initial conditions for the post-collapse bubble regime are as follows:

Post − Collapse
$x(t_c) = x_c$
$\dot{x}(t_c) = \frac{\rho A x_c v_{1c} + \rho A(L - x_c)v_{2c}}{\rho A L}$.

(11)

The 1D model provides a way to quickly estimate the net volume displaced per pulse (also known as the per pulse flow rate) and is a valuable first-order design tool for microfluidic systems utilizing thermal bubble-driven micro-pumps. This work analyzes the relationship between bubble strength, q_o, and pump size, A, to map the function $f = q_o(A)$ and provides a framework to predict the size of a thermal bubble-driven micro-pump needed to achieve a specified per pulse flow rate.

3. Materials and methods

3.1. Resistor and micro/mesofluidics design & fabrication

Laser cutting provides a way to rapidly fabricate single material, high-power resistors and micro/mesofluidic acrylic channels through a rapid non-fab process (by which we mean a non semiconductor

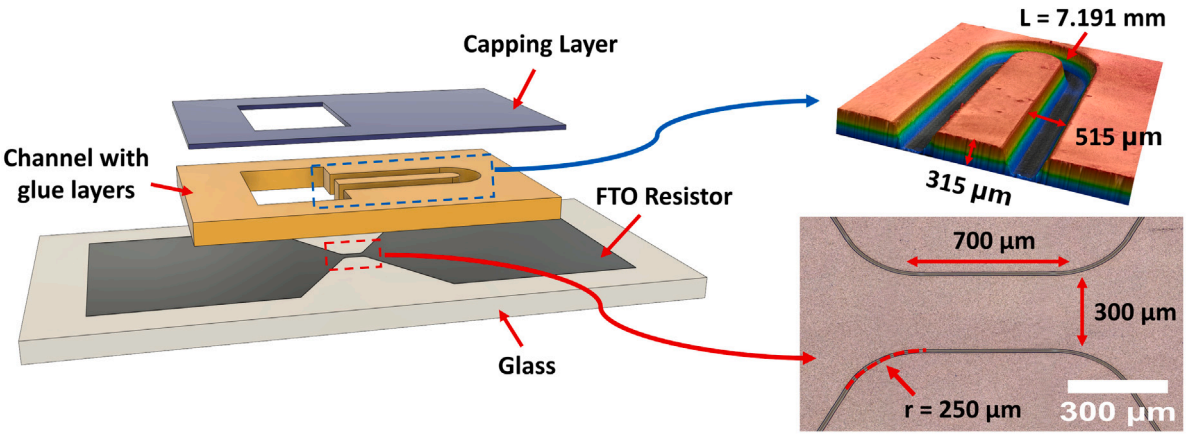

Fig. 2. Resistor and Micro/Mesofluidic Design & Fabrication — displays the design and fabrication of both resistor and micro/mesofluidic channel components of a thermal bubble-driven micro-pump. Devices are made using laminate processing in which FTO coated glass is laser cut to define the resistor region, a 200 µm acrylic sheet with 58.42 µm adhesive glue on both sides is manually aligned and pressed to the glass, and a 1 mm acrylic sheet is used to cap the open channels making the device water tight. Inset image 1, top right, illustrates a 3D Keyence confocal height map of the channel layer. Inset image 2, bottom right, illustrates a 2D Keyence confocal image of the resistor region (300 × 700 µm^2).

micro-fabrication workflow). Here, we use a 6DLasers laser micro-machine which has a Light Conversion CARBIDE-CB5 Femtosecond UV source, an ALIO 6D Hybrid Hexapod stage, and an integrated SCANLAB excelliSCAN galvanometer positioning system with a spot size of approximately 5 µm enabling a minimum resolution of structures on the order of 10's of µm. The detailed workflow and femtosecond laser processing parameters are described and characterized in our past work (Hayes et al., 2022).

Fig. 2 summarizes the design and fabrication process for a thermal bubble-driven micro-pump. Fusion 360 was used to design the resistor and channel geometries. Resistors were designed to target a range of rectangular dimensions (300 × 700 µm^2 in Fig. 2) and a 250 µm fillet for each corner was used to minimize hot spots near the edges of the resistor which can cause device failure (Bar-Levav et al., 2020). Once designed, resistors were fabricated by laser cutting commercial 8 Ω/sq, 340 nm fluorine-doped tin oxide (FTO) thin film coated glass (Sigma Aldridge, St. Louis, MO, USA). To define the micro/mesofluidic channels, a 58.42 µm glue layer (3M 467MP) was laminated to both sides of a 200 µm thick acrylic sheet (Emco Industrial Plastics) which was then manually aligned and pressed over the FTO resistor. A 1 mm thick acrylic sheet was used to cap the open channels making the device water tight. Femtosecond laser processing provides a non-fab method to rapidly fabricate thermal bubble-driven micro-pumps with near-fab resolution as shown by Keyence VK X-1100 optical profilometer images in Fig. 2 (top right and bottom right inset images). A U-shaped channel with a common reservoir was used to simplify the micro/mesofluidic setup as it ensured no pressure gradient between the two sides of the channel.

3.2. Electrical and imaging setup

Thermal bubble-driven micro-pumps are high-speed actuators in which bubble nucleation, expansion, and collapse occurs in less than 100 µs (Govyadinov et al., 2016; Hayes et al., 2022). Furthermore, bubble nucleation results from a high-power, rapid heating pulse lasting on the order of µs's. As such, custom electrical and imaging setups were utilized to deliver the transient heating pulses as well as perform stroboscopic high-speed imaging. The electrical setup used in this study is detailed in our past work (Hayes et al., 2022) and is capable of delivering 0–300 V, 0–5.6 A, 0.1–100 µs heating pulses. The electrical setup is time synced to a custom imaging setup in which a high intensity LED light source (Lightspeed Technologies HPLS-36DD18B) and a Basler CMOS camera with a global shutter (a2A1920-160 umBAS) is used to enable high resolution stroboscopic high-speed imaging. The

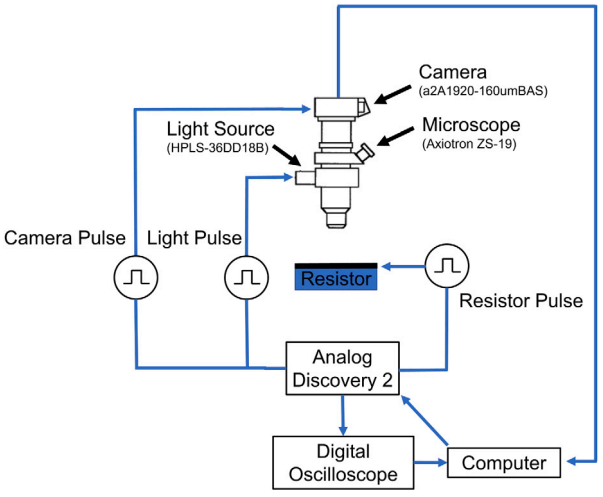

Fig. 3. Stroboscopic imaging setup — illustrates the custom stroboscopic imaging setup used to image vapor bubble dynamics and particle velocimetry data. The system is capable of imaging at up to 20 Mfps.

HPLS-36DD18B LED can be pulsed from 50 ns–2 µs at a 1% duty cycle which sets the maximum effective frame rate of the system at 20 Mfps. The imaging setup is shown in Fig. 3 and is described in detail in our past work (Hayes et al., 2022).

3.3. Particle tracking and flow rate measurement

To measure the flow rate, 1–10 µm and 27–32 µm diameter neutrally buoyant particles (Cospheric Inc., Goleta, CA, USA) were added to the channel reservoir and Lagrangian particle tracking was used to calculate the per pulse flow rate. For smaller channel dimensions, 1–10 µm particles were required to properly sample the flow; for larger channel dimensions, 27–32 µm particles were adequate. A MATLAB implementation of the interactive data language, IDL, particle tracking software (Crocker and Grier, 1996) was used to identify and track particle movement for each firing pulse. We follow the approach put forth from Kornilovitch et al. (2022) to better estimate the average velocity in a micro-channel by focusing the image plane on the center of the channel to record the particles with the fastest velocity and then using a 1:1 theoretical mapping between the maximum velocity and average velocity in a rectangular micro-channel to estimate the average

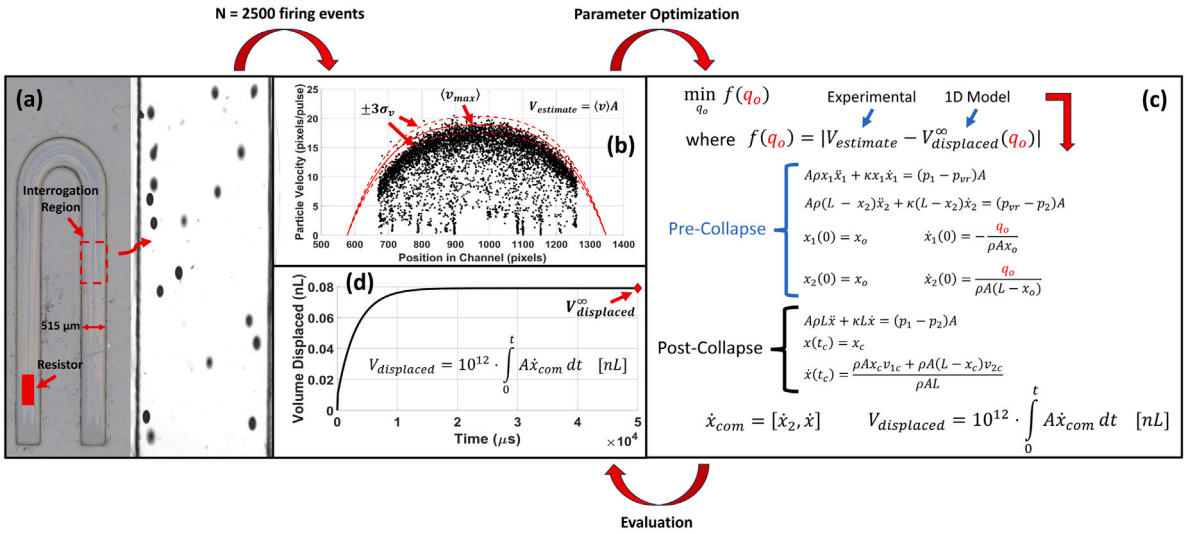

Fig. 4. Bubble strength computation — depicts the steps to estimate bubble strength from experimental particle tracking data. (a) particle tracking data is collected for a given resistor and channel geometry. (b) $N = 2500$ firing events are recorded to ensure sufficient statistics to estimate the average velocity in the channel and thus the volume displaced per pulse, denoted as $V_{estimate}$. (c) parameter optimization using MATLAB *fminsearch* algorithm is performed to find the needed bubble strength, q_o, such that the experimentally calculated volume displaced per pulse, $V_{estimate}$, matches that of the predicted volume displaced per pulse from the 1D model, denoted as $V^{\infty}_{displaced}$. (d) output from the 1D model with the final estimation of the bubble strength to match experimental data.

velocity. A complete discussion of this procedure is provided in our past work (Hayes et al., 2022).

3.4. Computation of bubble strength

Bubble strength, q_o, is the initial mechanical momentum imparted to both fluid columns as a result of the vapor bubble nucleation. Mathematically, the bubble strength appears in the initial conditions, Eq. (9), for the vapor bubble equations of motion, Eqs. (5)–(6). To estimate the bubble strength for a given resistor and channel geometry, the following steps are performed, shown graphically in Fig. 4:

1. *Particle Tracking*. Experimental particle tracking data is recorded with $N = 2500$ firing events, Fig. 4a.
2. *Estimate Volume Displaced per Pulse*. The maximum velocity is estimated from particle tracking statistics, Fig. 4b, and used to estimate the average velocity per pulse in the channel and thus the volume displaced per pulse (for a complete description see Kornilovitch et al., 2022 and Hayes et al., 2022).
3. *Solve for Bubble Strength*. Parameter optimization using MATLAB *fminsearch* is performed to compute the bubble strength such that the predicted volume displaced per pulse from the 1D model matches that of the experimental data, Fig. 4c-d.

We note that each computation of the bubble strength is based on $N = 2500$ experimental firing events to collect sufficient particle tracking statistics to estimate the average velocity and thus volume displaced per pulse for a given resistor and channel geometry.

4. Vapor bubble dynamics (Unconfined vs. Confined)

Vapor bubble dynamics of thermal bubble-driven micro-pumps directly determine pump performance. That is, the flow rate per pulse depends on the pressure of the initial vapor bubble, the degree of homogeneous vs. heterogeneous nucleation, the speed of vapor bubble expansion and collapse, and the maximum vapor bubble volume. Each parameter is influenced by the power and energy of a firing pulse. This is a complex parameter space. Past literature has shown that the heating rate determines the extent of homogeneous vs. heterogeneous nucleation during the onset of boiling (Einat and Grajower, 2010; Okuyama et al., 2006). In the ideal case, a thermal bubble-driven micro-pump makes use of a single, high pressure vapor bubble that forms uniformly over the surface of a resistor to perform mechanical work. However, if the heating rate is too high, the superheat energy at boiling incipient decreases which causes a smaller vapor bubble growth and thus less mechanical work; if the heating rate is too low, heterogeneous nucleation can occur resulting in multiple, lower pressure vapor bubbles instead of a single, high pressure vapor bubble that forms in the case of homogeneous nucleation (Okuyama et al., 2006). Thus, there is a tradeoff between the power and energy of a firing pulse. In this study, we fixed the firing pulse duration at $\tau = 5$ μs and varied the power to achieve different energies and heating rates. Determination of optimal firing pulse parameters is a crucial part of thermal bubble-driven micro-pumps operation and is discussed in the next section.

We found that additional complexity is introduced when vapor bubbles are confined in a closed channel. Fig. 5 compares unconfined vs. confined vapor bubble dynamics for a 300 × 600 μm^2 resistor with 250 μm corner fillets. The confined case utilizes a U-shaped channel shown in Fig. 2 in which the channel width, channel height, channel length, and resistor distance from reservoir were 366 μm, 329 μm, 7.191 mm, and 926 μm respectively. A firing pulse of P = 265 W was used to ensure consistency. As shown in Fig. 5, when confined, the vapor bubble breaks up instead of behaving as a single bubble like in the unconfined case. This is a different modality for thermal bubble-driven micro-pumps when compared to that on the micro-scale which will be the focus of future work. In the unconfined case, Fig. 5a, the vapor bubble nucleates around t = 3.5 μs and small bubbles quickly coalesce into a single vapor bubble which rapidly expands and collapses. Here, the vapor bubble expands against atmospheric pressure and follows a standard expansion, collapse, and post-collapse cavitation timeline observed in literature (Torniainen et al., 2012; Hayes et al., 2022; Ory et al., 2000). In the confined case, Fig. 5b, the vapor bubble nucleates around t = 3.5 μs and small bubbles quickly form distinct vapor regions, t = 4.5 μs, that break up as the vapor bubble grows, t = 10 μs. We hypothesize that the non-uniform heating zone and nucleation incipient at the resistor corners creates vapor bubble regions of different pressures which interact and cause the vapor bubble to break up. However, a detailed analysis of confined vapor bubble break up is beyond the scope of this study and will be the focus of future work. Nevertheless, it is important to note that vapor bubble dynamics are inherently different for unconfined vs. confined cases.

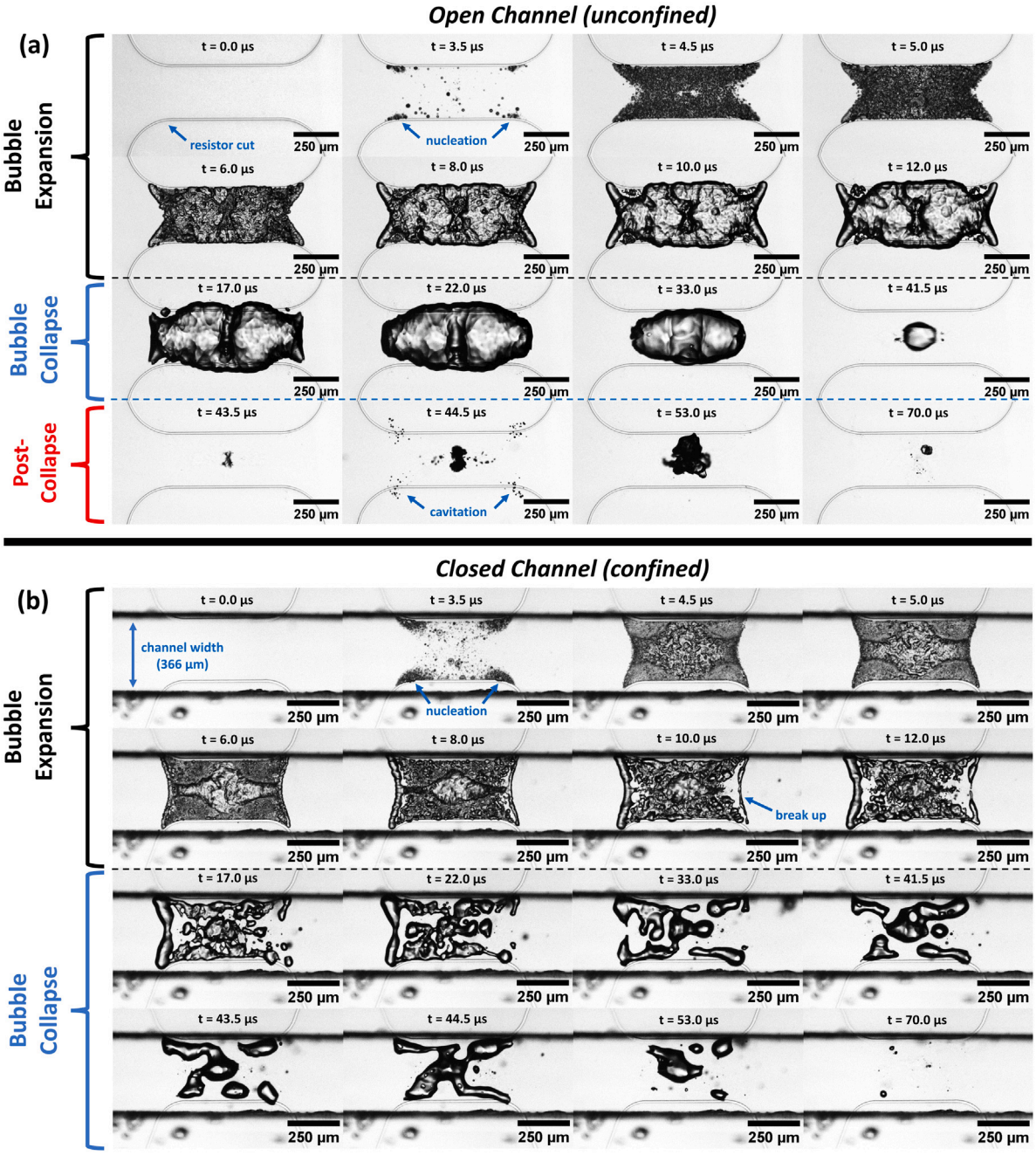

Fig. 5. Unconfined vs. Confined bubble dynamics — displays stroboscopic high speed imaging of vapor bubble dynamics for both open reservoir (unconfined) and closed channel (confined) case studies. In both cases, a firing pulse of P = 265 W was applied to 300 × 600 µm^2 resistors with 250 µm corner fillets. In (a), water was placed on the surface of a 300 × 600 µm^2 resistor and bubble dynamics were imaged. Bubble nucleation occurs at t = 3.5 µs upon which the vapor film rapidly coalesces and expands until reaching its maximum extent, t = 17.0 µs, upon which the vapor bubble collapses. Vapor bubble collapse creates a cavitation event, t = 44.5 µs, which causes vapor bubble rebound. In (b), a U-shaped channel, as shown in Fig. 2, was placed over the resistor and filled with water in which the channel width, channel height, channel length, and resistor distance from reservoir were 366 µm, 329 µm, 7.191 mm, and 926 µm respectively. Bubble nucleation occurs at t = 3.5 µs upon which the vapor film expands and forms distinct regions, t = 6.0 µs. During expansion, the bubble breaks up, t = 10.0 µs, and begins to collapse at t = 17.0 µs until it fully collapses without bubble rebound at a t = 70 µs. Stroboscopic imaging was performed at 2 Mfps.

5. Scaling analysis

5.1. Resistor firing parameters

Optimal resistor firing parameters (pulse duration and voltage) are critical for operation of thermal bubble-driven micro-pumps. If too little energy, the vapor bubble will be underdriven resulting in little to no flow; if too much energy, the vapor bubble will be overdriven and the thin film resistor will burnout. As such, it is important to map the optimal firing parameters to avoid underdriving or overdriving FTO thin film resistors across size scales. In this study, the peak current density is used as a metric of the energy input,

$$J = \frac{I}{wt_f} = \frac{V/R}{wt_f} \tag{12}$$

where I is the bulk current, w is the resistor width, t_f is the thickness (340 nm in the case of FTO 8 Ω/sq glass), V is the voltage, and R is the total resistance. We utilized a 5 µs pulse duration and varied the voltage to change the peak current density. Theoretically, an ideal rectangular TIJ resistor would exhibit energy saturation in which the

vapor bubble grows up to a certain limit upon which additional energy results in negligible gains in the vapor bubble area and observed flow rate. This saturation phenomenon, known as vapor lock, occurs when the entire fluid layer in contact with the resistor's surface vaporizes creating a vapor blanket that insulates the hot resistor from the rest of the fluid. Once the vapor blanket forms, any further increase in resistor temperature does not result in additional heat transfer to the fluid (Kornilovitch et al., 2022). In this case, the max bubble area as a function of peak current density would follow a Sigmoid function which is bounded,

$$S_1(J) = \frac{a}{1 + be^{-c(J-d)}} \tag{13}$$

where J is the peak current density, and $\{a, b, c, d\}$ are model fitting parameters. However, in this study, we use resistor designs with filleted edges to reduce current crowding and burnout, which results in a non-uniform heating zone, see Fig. 2. Thus, additional energy input causes the effective bubble nucleation zone to increase in area which results in a monotonically increasing max bubble area as a function of peak current density. Fig. 6 shows this behavior across different size FTO 8 Ω/sq resistors ranging from A = width × height = 100 × 200 μm^2 to A = 450 × 900 μm^2. Water is placed over the resistor's surface, which we denote as an "open channel" or "unconfined" configuration meaning the resistor is not confined to a channel. The peak current density is used as a metric to indicate underdriven, transition, optimal, and overdriven vapor bubble regimes colored red, yellow, green, and red from left to right respectively. Inset images display the vapor bubble as it progresses from underdriven to overdriven for the A = 400 × 800 μm^2 resistor. To quantify the firing conditions independent of resistor area, the max bubble area is normalized at the largest common peak current density tested across all sizes. Instead of a bounded Sigmoid function to model the vapor bubble growth as a function of energy input, a parameterized inverse hyperbolic sine function is used which is unbounded,

$$S_2(J) = a \cdot log\left((J - c) + \sqrt{b + (J - c)^2}\right) \tag{14}$$

where J is the peak current density, and $\{a, b, c\}$ are model fitting parameters. Fig. 7 shows the max normalized bubble area as a function of peak current density. It can be seen that the max normalized bubble area is independent of resistor size. As such, the fitted inverse hyperbolic sine function is used to define vapor bubble operating regimes. Underdriven is defined as $S_2 < 0.08$, transition is defined as $0.08 < S_2 < 0.90$, optimal is defined as $0.90 < S_2 < 0.95$, and overdriven is defined as $S_2 > 0.95$ where S_2 is the max normalized bubble area fitted inverse hyperbolic sine function. Thus, the optimal firing condition, $0.90 < S_2 < 0.95$, corresponds to peak current densities of $2.11 \times 10^{10} < J < 2.29 \times 10^{10}$ A/m^2 which is utilized throughout this study to ensure a fully developed vapor bubble.

5.2. Frequency dependence of pumping

Commercial thermal bubble-driven micro-pump resistors can operate at firing frequencies up to 10's of kHz without substantial heat buildup due to their small size scale (10's μm) and silicon substrate to remove heat from the system after a firing pulse (Torniainen et al., 2012). However, in this study, we utilize large resistors (100's μm) on a glass substrate in which the heat buildup per firing pulse can be significant. The thermal conductivity of silicon is approximately 148 times higher than that of glass (k = 148 $\frac{W}{m\,K}$ for silicon vs. k = 1 $\frac{W}{m\,K}$ for glass. As such, for resistors in this studied made with a glass substrate, residual heat causes the initial resistor temperature to increase which, in turn, causes the nucleation temperature to increase and thus the micro-pump flow rate will be dependent on the firing rate.

This phenomenon can be demonstrated through a lumped-capacitance 1D heat conduction model of the resistor. Resistive heating in thermal bubble-driven micro-pumps can be modeled using 1D heat conduction, due to the high heating rates on the order of 100 °C/μs (Okuyama et al., 2006), with two stages: (1) heating and (2) cool down. During the heating stage, the applied voltage pulse causes rapid heating of the resistor as detailed in Eq. (15)

$$\rho_s \mathcal{V} c_p \frac{dT_h}{dt} = \frac{V_{app}^2}{R} - hA(T_h - T_\infty) \tag{15}$$

with initial condition of $T_h(0) = T_o$ where ρ_s is the resistor material density, $\mathcal{V}$ is the heater volume, c_p is the specific heat capacity, T is the temperature, t is the time, V_{app} is the applied voltage, R is the resistance, h is the heat transfer coefficient, A is the top-down resistor area, T_∞ is the temperature of the fluid, and T_o is the initial resistor temperature. Similarly, the cool down stage is modeled as

$$\rho_s \mathcal{V} c_p \frac{dT_c}{dt} = -hA(T_c - T_\infty) \tag{16}$$

with initial condition of $T_c(\tau) = T_h(\tau)$ where τ is the heating pulse duration and the initial condition is coupled to the final temperature at the end of the heating stage. In this study, the resistive heater is made from FTO with a density of 7120 kg/m^3, specific heat capacity of 341 J/(kg K), and film thickness of 340 nm. For this canonical example, we consider a 300 × 700 μm^2 resistor with resistance of 44.8 Ω upon which a heating pulse of 20 V is applied for 5 μs. The resistor temperature starts at ambient and rapidly increases due to Joule heating until the voltage pulse ends and the resistor's surface cools down at a decay rate set by the heat transfer coefficient. It is difficult to experimentally determine the heat transfer coefficient for this system since the heat transfer coefficient is time dependent and greatly affected by the presence of vapor over the resistor (Ruiz, 2007). As such, for the purpose of this example, we consider the heat transfer coefficient constant at 5 W/(m^2 K). We note that this selection is arbitrary and chosen such that simulated temperatures are close to what would be expected for TIJ resistors. For this hypothetical resistive heater, a firing frequency of 1 Hz provides sufficient time for the resistor to fully cool down after each pulse, Fig. 8a. However, if the firing frequency is increased such that the resistor fails to fully cool down after each firing pulse, each subsequent pulse will add residual heat to the system until a new thermal steady-state condition is reached, Fig. 8b.

This mechanism acts to both increase the resistor temperature as well as pre-heat the bulk liquid around the resistor which will result in a stronger vapor bubble at the onset of nucleation; that is, the initial pressure of the vapor bubble will be larger due to a larger nucleation temperature which in turn will yield an increased flow rate (Kornilovitch et al., 2022). This phenomenon is observed experimentally, Fig. 9, in which the flow rate as a function of firing frequency is measured for three meso-scale thermal bubble-driven micro-pumps (300 × 600, 400 × 800, and 500 × 1000 μm^2). As the firing frequency increases, the flow rate per pulse also increases. To ensure consistency throughout this study, thermal bubble-driven micro-pumps were pulsed at 10 Hz unless otherwise specified.

5.3. Maximum firing frequency for linear operation

The maximum theoretical firing frequency for a thermal bubble-driven micro-pump to operate linearly can be described in two ways: (1) the time required for a vapor bubble to re-dissolve back into the subcooled liquid and (2) the time required for fluid motion to fully extinguish before the next firing pulse. Thermal bubble-driven micro-pumps operating in the linear regime implies that the *per pulse* flow rate is constant across firing frequency; that is, each firing pulse results in a consistent, unit amount of fluid displacement. This mode of operation enables a high degree of controlability and predictability for these micro-pumps. However, the linear operating regime is only obtained if the firing frequency allows for a delay time that is below both aforementioned conditions (1) and (2). Otherwise, the remnant vapor bubble, as in (1), or fluid motion, as in (2), from the previous firing pulse will affect the next pump cycle resulting in a decay in the *per pulse* flow rate (Govyadinov et al., 2016). In a practical micro/mesofluidic

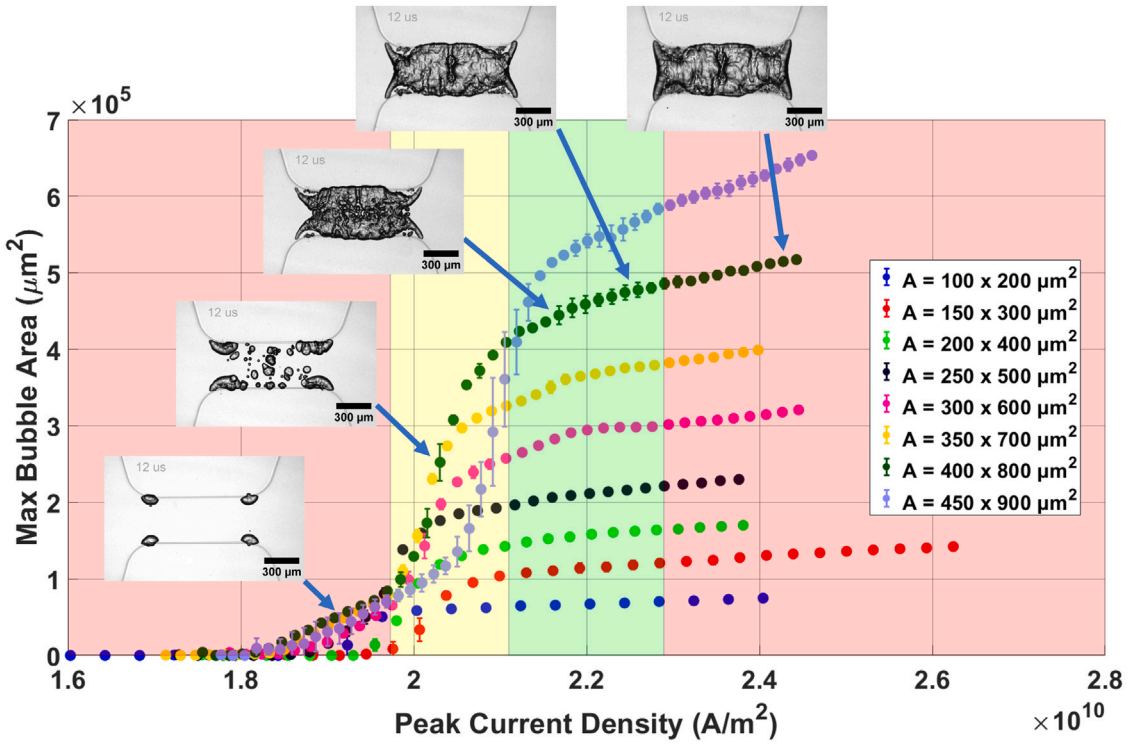

Fig. 6. Open channel firing conditions — displays the max bubble area as a function of peak current density for different size FTO resistors. The peak current density is used as a metric to indicate underdriven, transition, optimal, and overdriven vapor bubble regimes colored red, yellow, green, and red from left to right respectively. Operating regimes are further defined in Fig. 7. Inset images show the maximum vapor bubble for the 400 × 800 µm² case as it progresses from underdriven to overdriven. Each sample point was performed in triplicate. (For interpretation of the references to color in this figure legend, the reader is referred to the web version of this article.)

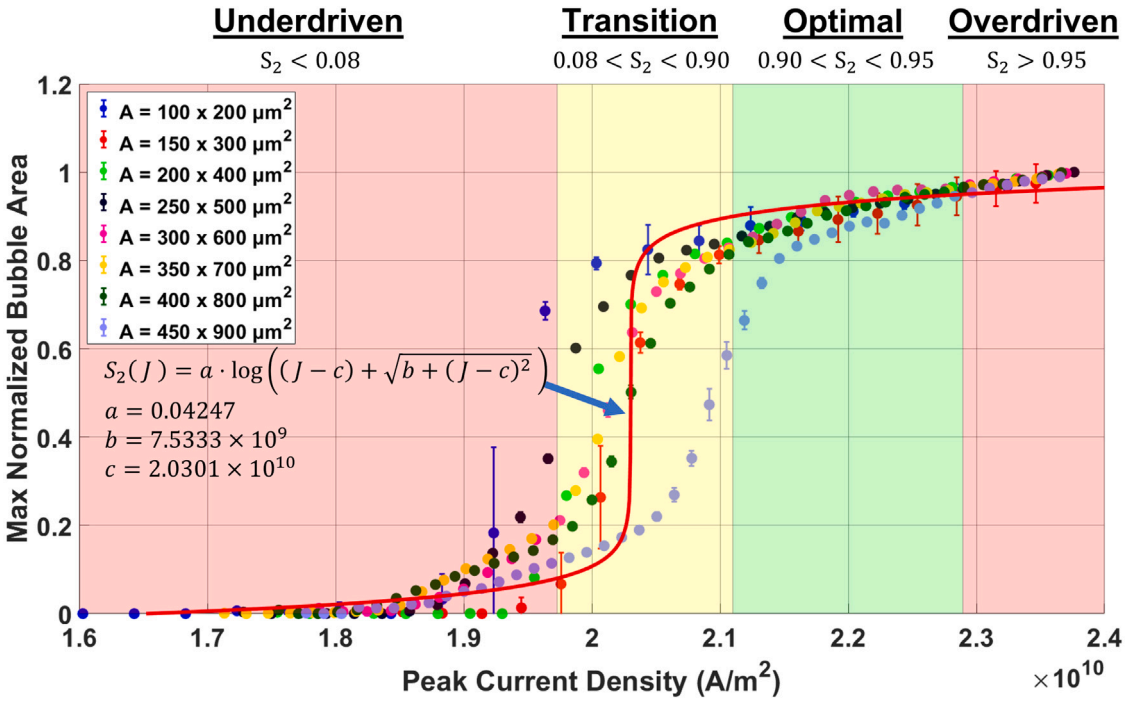

Fig. 7. Open channel firing conditions normalized — displays the max *normalized* bubble area as a function of peak current density for different size FTO resistors. The max bubble area is normalized at the largest common peak current density tested across all sizes. A parameterized inverse hyberbolic sine function is used to fit the data and identify operating vapor bubble regimes. The optimal firing condition was selected as $0.90 < S_2 < 0.95$ to avoid resistor burnout which corresponds to peak current densities of $2.11 \times 10^{10} < J < 2.29 \times 10^{10}$ A/m². Each sample point was performed in triplicate.

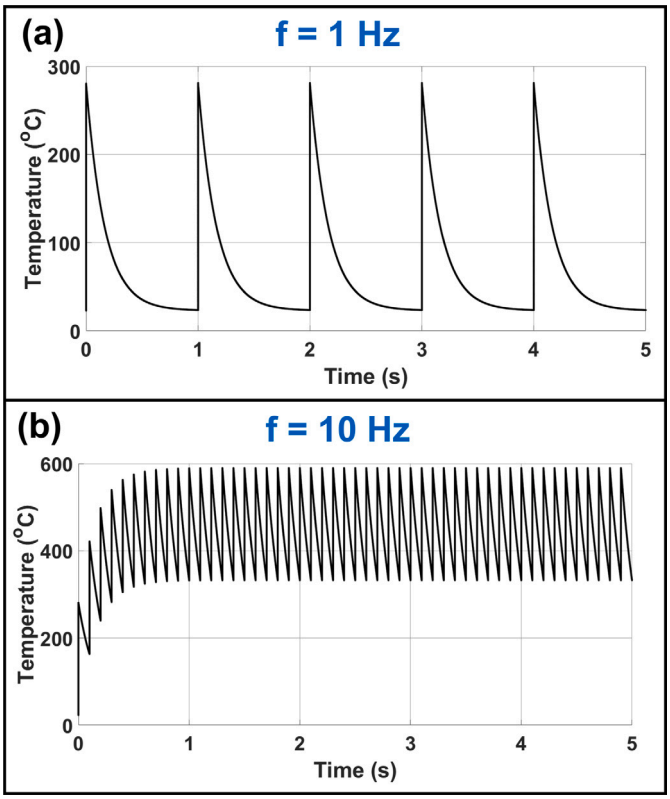

Fig. 8. 1D Heat conduction model for frequency dependence of resistive heating — illustrates the proposed mechanism of flow rate dependency on firing frequency in thermal bubble-driven micro-pumps. A 300 × 700 μm^2 FTO resistive heater (44.8 Ω) with a density of 7120 kg/m^3, specific heat capacity of 341 J/(kg K), and film thickness of 340 nm is modeled using Eqs. (15) and (16). A heating pulse of 20 V is applied for 5 μs and a constant heat transfer coefficient of 5 W/(m^2 K) is used. (a) depicts N = 5 pulses at a firing frequency of 1 Hz while (b) depicts N = 50 pulses at a firing frequency of 10 Hz. Residual heat buildup leads to an increased base temperature when the firing frequency exceeds the time required to fully cool down.

system with thermal bubble-driven micro-pumps, it may be unavoidable or even intended to operate in the non-linear regime; thus, it is important to understand where these micro-pumps transition from linear to non-linear operation.

We start with condition (1). Fig. 10a depicts the maximum firing frequency as a function of resistor area derived from the vapor bubble collapse time for operation in the linear regime. Specifically, the maximum firing frequency is defined as the inverse of the time required for the vapor bubble to fully collapse, as shown in the inset in Fig. 10a. Both open channel, defined as when a pool of water is placed over a resistor, and closed channel, defined as when a resistor is confined in a micro/meso-channel, geometries were used with dimensions specified in Appendix B. We find that although the shape of the bubble area vs. time graph differs for open vs. closed channel devices (see past work Hayes et al., 2022), the vapor bubble collapse time is similar. We hypothesize that this mechanism is due to the vapor bubble initializing with a similar temperature and pressure regardless of if it is unconfined or confined to a channel. In Fig. 10a, linear operation is specified as all points below the power law curve fit, shown in green, and non-linear operation is specified as all points above the power law curve fit, shown in yellow.

With respect to condition (2), Fig. 10b depicts the maximum firing frequency as a function of resistor area derived from the fluid extinction time for operation in the linear regime. Specifically, the maximum firing frequency is defined as the inverse of the predicted time from the 1D model, see Eqs. (4)–(10), for the fluid motion to fully extinguish (reaching 1% of the final volume displaced) due to viscosity, as shown in the inset in Fig. 10b. Channel and resistor geometry dimensions are specified in Appendix B. In Fig. 10b, linear operation is specified as all points below the power law curve fit, shown in green, and non-linear operation is specified as all points above the power law curve fit, shown in yellow. We note that the time required for fluid motion to extinguish is significantly longer than the time required for the vapor bubble to fully re-dissolve back into the subcooled liquid, 100's μs vs. 10,000's μs, unlike the case for micro-scale geometries studied by Govyadinov et al. (2016) This effect is due to the fluidic resistance scaling with $1/d^4$ as described below for a circular channel

$$R_{fluidic} = \frac{128\mu L}{\pi d^4} \tag{17}$$

where μ is the viscosity, L is the channel length, and d is the diameter. As such, the secondary pumping effect is dominant in mesofluidic systems with thermal bubble-driven micro-pumps since it takes longer for viscosity to extinguish fluid motion. To operate in the linear regime, meso-scale thermal bubble-driven micro-pumps can only operate at frequencies on the order of 25–100 Hz depending on the resistor area, Fig. 10b.

For commercial devices, it is expected that meso-scale thermal bubble-driven micro-pumps may need to pulse faster than 100 Hz to achieve desired flow rates. As a result, additional study will be required to understand the decay in *per pulse* flow rate for meso-scale thermal bubble-driven micro-pumps, which is beyond the scope of this current study and left for future work.

5.4. Bubble strength as a function of resistor size

The flow rate *per pulse* of thermal bubble-driven micro-pumps depends on resistor area, channel geometry, and electrical firing parameters. In this study, we use fully developed vapor bubbles, as discussed in Section 5.1, in order to reduce the flow rate dependency to resistor and channel geometric dimensions. The channel cross-section affects the fluidic resistance and thus greatly influences the resulting flow rate; similarly, as the channel length increases, additional fluid mass causes the flow rate to decrease (Kornilovitch et al., 2022). To more generally characterize the pumping performance of thermal bubble-driven micro-pumps, we follow the convention put forth from Kornilovitch et al. in which the characteristic bubble strength q_o, defined in Eq. (4), is used to represent the momentum imparted to the fluid thus making this phenomenological parameter independent of channel geometry (Kornilovitch et al., 2022, 2013). Here, five resistors of areas 100 × 200, 200 × 400, 300 × 600, 400 × 800, and 500 × 1000 μm^2 were placed in meso-channels with design widths equal to the resistor design width plus 50 μm tolerance and channel heights approximately 342 μm. The resistor position from the edge of the reservoir, channel width, channel height, and channel length were measured using a Keyence VK X-1100 optical profilometer. For a complete list of dimensional data for resistors and channels, see Appendix B. Particles were seeded in the fluid and a custom optical microscope setup was used to perform particle tracking to measure the flow rate for each resistor and channel design. Once the flow rate *per pulse* was estimated, see Section 3.3, Eqs. (4)–(10) were cast as a least-squares optimization problem to estimate the bubble strength, q_o. For each resistor area, three different channel lengths of the same cross-section were used in order to better estimate the bubble strength as done by Kornilovitch et al. since the bubble strength is invariant of the channel length (Kornilovitch et al., 2022).

Fig. 11 illustrates the dependence of the bubble strength, q_o, on the resistor area. As expected, the bubble strength linearly increases with the resistor area. In this study, resistors with areas spanning three orders of magnitudes from micro-scale to meso-scale were used to predict the scaling relationship of bubble strength. The 15 × 33.3 μm^2 resistor data was taken from work done by Govyadinov et al. on micro-scale thermal bubble-driven micro-pumps (Govyadinov et al., 2016). Specifically, we find the following empirical linear relationship

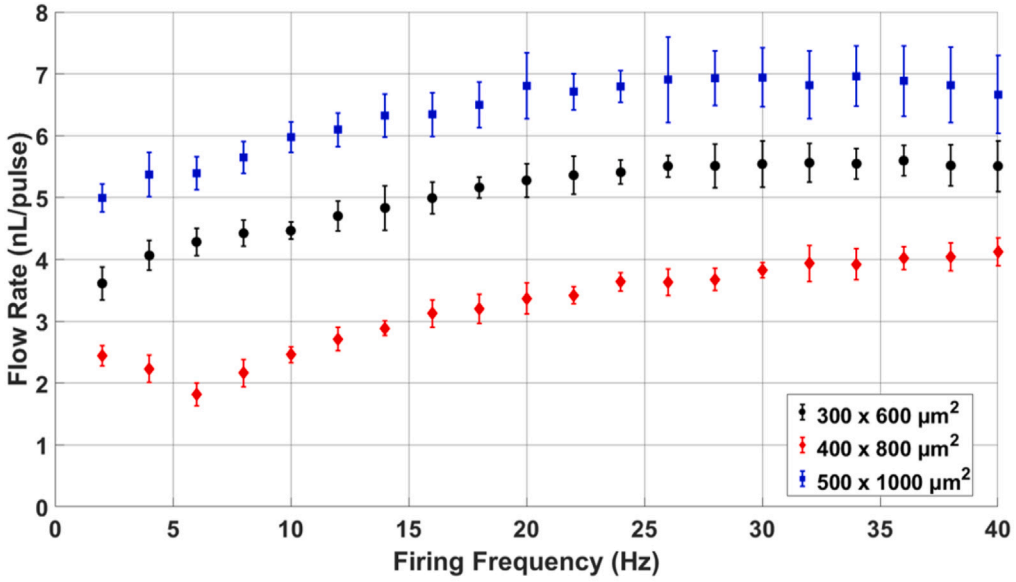

Fig. 9. Frequency dependence of pumping — illustrates the dependence of flow rate per pulse on the resistor firing frequency. The 300 × 600 μm² resistor was placed 926 μm from the inlet of a U-shaped 366 × 329 μm² (width × height) rectangular channel of length, L = 7.191 mm. The 400 × 800 μm² resistor was placed 1563 μm from the inlet of a U-shaped 469 × 332 μm² rectangular channel of length, L = 10.105 mm. The 500 × 1000 μm² resistor was placed 1752 μm from the inlet of a U-shaped 573 × 332 μm² rectangular channel of length, L = 11.558 mm. Flow rate data was recorded for N = 2500 firing events for each firing frequency. Each firing frequency sample was performed in triplicate.

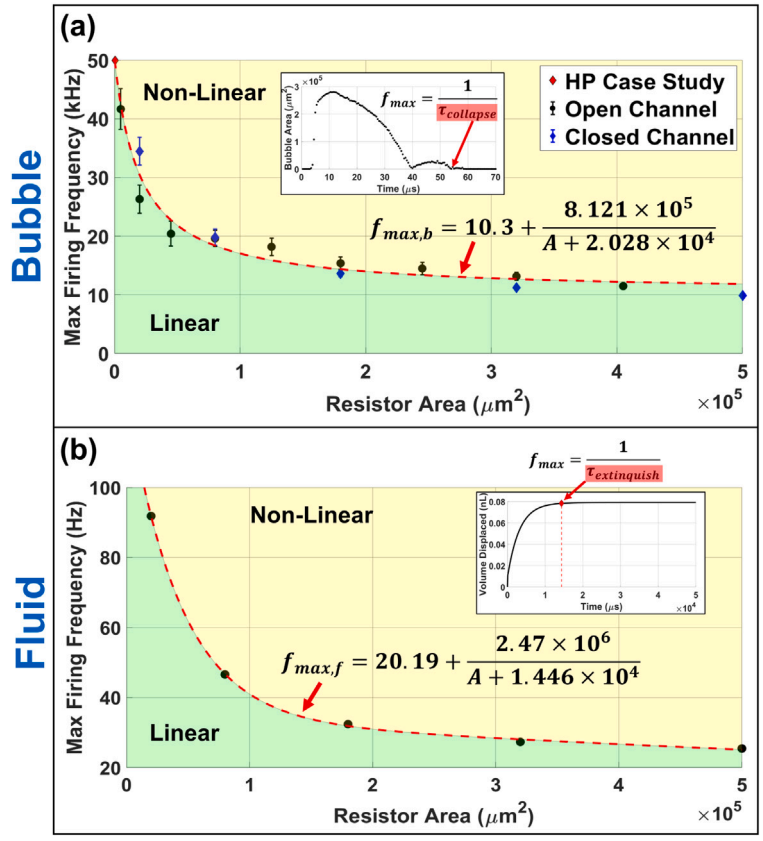

Fig. 10. Operating mode of meso-scale resistors — illustrates the maximum firing frequency to operate in the linear and non-linear regimes as a function of resistor area. In (a), the collapse time of a vapor bubble is used to set the linear vs. non-linear regime for the maximum firing frequency to ensure vapor bubbles do not overlap in time. The inset image defines the collapse time for a vapor bubble from a 100 × 200 μm² resistor in the open channel configuration. Open channel resistor areas were 50 × 100, 100 × 200, 200 × 400, 300 × 600, 400 × 800, and 500 × 1000 μm². Closed channel resistor areas were 100 × 200, 200 × 400, 300 × 600, 400 × 800, and 500 × 1000 μm² with channel dimension defined in Appendix B. In (b), the extinguish time required for fluid motion to stop, defined as when the volume displaced per pulse is within 1% of the final volume displaced, is used to set the linear vs. non-linear regime for the maximum firing frequency to ensure firing pulses do not overlap in time. Resistor areas were 100 × 200, 200 × 400, 300 × 600, 400 × 800, and 500 × 1000 μm² with channel dimension defined in Appendix B. The inset image defines the extinguish time for fluid based on 1D model volume displaced simulations from a 100 × 200 μm² resistor. Each resistor was tested in triplicate in which error bars are one standard deviation from the mean. (For interpretation of the references to color in this figure legend, the reader is referred to the web version of this article.)

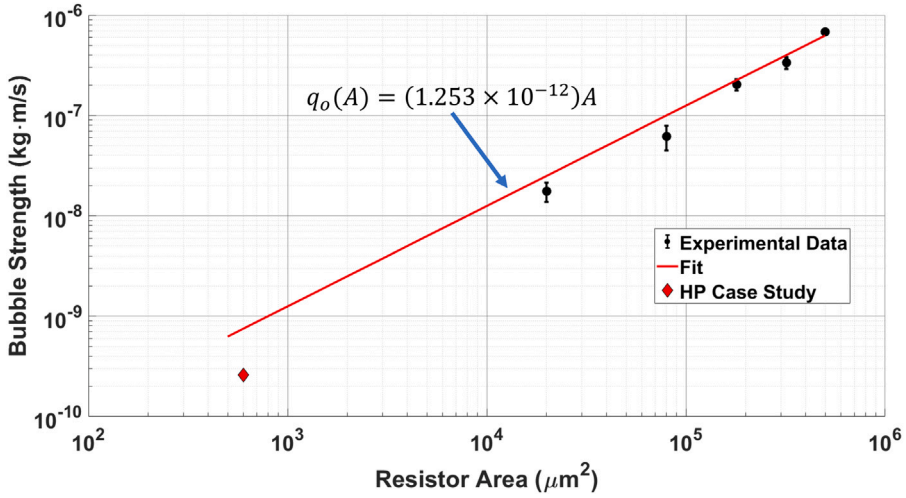

Fig. 11. Bubble strength dependence on resistor area — describes the dependence of the bubble strength, q_o, on the resistor area. Each resistor area design was tested in triplicate with 3 different channel lengths to compute an average bubble strength using the 1D model. Specifically, Eqs. (4)–(10) were cast as a least-squares optimization problem to estimate the bubble strength, q_o. The 15×33.3 μm^2 resistor case study is included based on data from Govyadinov et al. (2016) The firing frequency was 10 Hz across all tests and $N = 2500$ firing events was used to determine the *per pulse* flow rate for each test. The y-intercept of the model fit was forced to zero in order to better approximate the bubble physics; that is, a resistor of zero area will have zero bubble strength. The R^2 value is 0.96.

between bubble strength, q_o [kg m/s], and the resistor area, A [m^2], with the fitting constant, k [$\frac{\text{kg}}{\text{m s}}$]:

$$q_o(A) = kA = \left(1.253 \times 10^{-12}\right) A. \tag{18}$$

To our knowledge, this is the first work that describes the empirical relationship between bubble strength and resistor area in an attempt to make the reduced parameter 1D model of thermal bubble-driven micro-pumps more generalized. Instead of requiring experimental data to estimate the bubble strength for a particular microfluidic channel with a thermal bubble-driven micro-pump of a given area, this work provides an estimate for the bubble strength as a function of the resistor area thus eliminating the need for experimental data to perform a first-order analysis of thermal bubble-driven micro-pumps.

6. Conclusions

Thermal bubble-driven micro-pumps are an upcoming micro-pump technology to move fluid at the micro to meso-scale without any moving parts and can be integrated directly into micro/mesofluidic channels showing great promise to enable true "lab-on-a-chip" technologies. For instance, these integrated micro-pumps could play a crucial role in single cell isolation, cell sorting, cell lysing, and even microfluidic mixing. In this work, a comprehensive scaling analysis is performed ranging from the resistor firing parameters to the effect of resistor area on flow rate in order to study the frequency dependence of pumping, the maximum firing frequency for micro to meso-scale resistors to operate in the linear regime, and derive an empirical relationship between bubble strength and resistor area. Specifically, it was found that the per pulse flow rate increased as the resistor firing frequency increased (an approximate 1.4X increase from 2 Hz to 35 Hz for a 300×700 μm^2 resistor). The flow rate dependency on firing frequency was hypothesized to be due to residual heat buildup within the substrate of the micro-pumps. Additionally, it was found that it took approximately 100X longer for fluid motion to be extinguished in meso-scale devices than that at the micro-scale which is to be expected due to scaling of the fluidic resistance. Lastly, it was found that the following empirical scaling law describes the bubble strength as a function of resistor area: $q_o(A) = (1.253 \times 10^{-12})A$ [kg m/s], which had an R^2 value of 0.96. Moreover, the developed empirical scaling law of bubble strength as a function of resistor area allows for the 1D model describing thermal bubble-driven micro-pumps to be used without the need for experimental data as was previously required. With use of this scaling law, we envision the reduced parameter 1D model as a first-order design tool for microfluidic designers to rapidly predict the size of a thermal bubble-driven micro-pump needed for a desired flow rate.

CRediT authorship contribution statement

Brandon Hayes: Conceptualization, Investigation, Visualization, Validation, Data curation, Writing – original draft. **Kaushik Jayaram:** Hardware, Methodology, Supervision, Writing – review & editing. **Robert MacCurdy:** Conceptualization, Methodology, Writing – review & editing, Supervision, Funding acquisition.

Declaration of competing interest

The authors declare the following financial interests/personal relationships which may be considered as potential competing interests: Robert MacCurdy reports financial support was provided by University of Colorado Boulder College of Engineering and Applied Science. Brandon Hayes reports financial support was provided by National Science Foundation.

Data availability

Data will be made available on request.

Acknowledgments

The authors would like to thank Pavel Kornilovitch and Alex Govyadinov for insights and fruitful discussions of this work.

This work is supported by startup funds to R. MacCurdy provided by the University of Colorado Boulder as well as the National Science Foundation Graduate Research Fellowship under Grant No. DGE 1650115. Any opinion, findings, and conclusions or recommendations expressed in this material are those of the author(s) and do not necessarily reflect the views of the National Science Foundation.

Table B.1
Resistor and channel dimensions — key resistor and channel dimensions used in this study are reported for completeness and reproducibility. Dimensional data for resistors and micro/meso-channels used in Fig. 9 as well as Fig. 10 are illustrated. Distance from reservoir, x_o, is defined as the distance from the reservoir to the midpoint of the resistor (see Fig. 1a). Data from Fig. 10 is color coded according to each repetition used in the study to estimate the bubble strength. For each resistor area, three different channel lengths of the same cross-section were used in order to better estimate the bubble strength as done by Kornilovitch et al. since the bubble strength is invariant of the channel length (Kornilovitch et al., 2022).

Fig. 9 – Frequency dependence of pumping					
Resistor		Channel			
Width (μm)	Length (μm)	Width (μm)	Height (μm)	Length (mm)	Distance from Reservoir, x_o (μm)
300	600	366	329	7.191	926
400	800	469	329	10.105	1563
500	1000	573	332	11.558	1752
Fig. 10 – Operating mode of meso-scale resistors					
Resistor		Channel			
Width (μm)	Length (μm)	Width (μm)	Height (μm)	Length (mm)	Distance from Reservoir, x_o (μm)
100	200	194	342	3.947	322
200	400	269	343	5.477	404
300	600	361	336	7.791	1003
400	800	467	340	8.105	859
500	1000	574	336	8.388	986
100	200	150	329	2.974	390
200	400	254	343	4.677	586
300	600	367	330	7.191	926
400	800	469	332	10.105	1563
500	1000	573	332	11.588	1752
100	200	149	340	2.574	256
200	400	245	332	4.077	408
300	600	367	336	8.791	693
400	800	469	336	9.105	803
500	1000	551	335	10.188	1168

Appendix A. Calculation of κ for a rectangular channel of cross-sectional area a × b

Here, we follow the derivation for the viscous stress dissipation factor κ put forth by Kornilovitch et al. (2013) and apply it to a rectangular channel cross-section. Let a and b be the rectangle dimensions along the y and z axis respectively. The series solution for the velocity profile and flow rate are given by the following expressions (Timoshenko and Goodier, 1970):

$$V_x(y,z) = \frac{\Delta P}{\mu L}\frac{16}{ab}\sum_{n,m=0}^{\infty}\frac{sin(p_{2n+1}y)sin(q_{2m+1}z)}{p_{2n+1}q_{2m+1}\left(p_{2n+1}^2+q_{2m+1}^2\right)} \tag{A.1}$$

$$Q = \frac{\Delta P}{\mu L}\frac{64}{ab}S_1(a,b) \tag{A.2}$$

where

$$p_{2n+1} = \frac{\pi(2n+1)}{a} \tag{A.3}$$

$$q_{2m+1} = \frac{\pi(2\ m+1)}{b} \tag{A.4}$$

$$S_1(a,b) = \sum_{n,m=0}^{\infty}\frac{1}{p_{2n+1}q_{2m+1}\left(p_{2n+1}^2+q_{2m+1}^2\right)}. \tag{A.5}$$

The velocity profile can be re-written in terms of the average velocity, $\langle v\rangle$ = Q/A.

$$V_x(y,z) = \langle v\rangle\frac{ab}{4S_1}\sum_{n,m=0}^{\infty}\frac{sin(p_{2n+1}y)sin(q_{2m+1}z)}{p_{2n+1}q_{2m+1}\left(p_{2n+1}^2+q_{2m+1}^2\right)} \tag{A.6}$$

Calculation of the viscous stress tensor and integrating over the wall perimeter gives the total viscous force which can be re-written as F = $\kappa\langle v\rangle L$ to agree with the one-dimensional model. In the case of a rectangular channel cross-section (Timoshenko and Goodier, 1970),

$$\kappa = ab\mu\frac{S_2(a,b)}{S_1(a,b)} \tag{A.7}$$

where

$$S_2(a,b) = \sum_{n,m=0}^{\infty}\frac{1}{\left(p_{2n+1}^2q_{2m+1}^2\right)}. \tag{A.8}$$

Appendix B. Dimensions of channels and resistors tested

A full list of resistor and channel dimensions used in this paper are provided in Table B.1 for completeness.

References

Bar-Levav, E., Witman, M., Einat, M., 2020. Thin-film MEMS resistors with enhanced lifetime for thermal inkjet. Micromachines 11 (5), URL https://www.mdpi.com/2072-666X/11/5/499.

Borgnakke, C., Sonntag, R.E., 1999. Fundamentals of Thermodynamics 8th Edition. Wiley.

Crocker, J.C., Grier, D.G., 1996. Methods of digital video microscopy for colloidal studies. J. Colloid Interface Sci. 179 (1), 298–310, URL https://www.sciencedirect.com/science/article/pii/S0021979796902179.

Davies, M., Abubaker, M., Bible, L., 2020. A flexible, microfluidic, dispensing system for screening drug combinations. Micromachines 11 (10), URL https://www.mdpi.com/2072-666X/11/10/943.

Duffy, D., Gillis, H., Lin, J., Sheppard, N., Kellogg, G., 1999. Microfabricated centrifugal microfluidic systems: Characterization and multiple enzymatic assays. Anal. Chem. 71.

Einat, M., Grajower, M., 2010. Microboiling measurements of thermal-inkjet heaters. J. Microelectromech. Syst. 19.

Govyadinov, A., Kornilovitch, P., Markel, D., Torniainen, E., 2016. Single-pulse dynamics and flow rates of inertial micropumps. Microfluid. Nanofluid. 20.

Hassan, S., Zhang, X., 2020. Design and fabrication of capillary-driven flow device for point-of-care diagnostics. Biosensors 39.

Hayes, B., Smith, L., Kabutz, H., Hayes, A.C., Whiting, G.L., Jayaram, K., MacCurdy, R., 2022. Rapid fabrication of low-cost thermal bubble-driven micro-pumps. Micromachines 13 (10), URL https://www.mdpi.com/2072-666X/13/10/1634.

Hayes, B., Whiting, G.L., MacCurdy, R., 2021. Modeling of contactless bubble–bubble interactions in microchannels with integrated inertial pumps. Phys. Fluids 33 (4), 042002, arXiv:https://doi.org/10.1063/5.0041924.

Hayes, B., Whiting, G.L., MacCurdy, R., 2023. An OpenFOAM framework to model thermal bubble-driven micro-pumps. Phys. Fluids 35 (6), 062013, arXiv:https://pubs.aip.org/aip/pof/article-pdf/doi/10.1063/5.0155615/18016336/062013_1_5.0155615.pdf.

Hirt, C., Nichols, B., 1981. Volume of fluid (VOF) method for the dynamics of free boundaries. J. Comput. Phys. 39 (1), 201–225, URL http://www.sciencedirect.com/science/article/pii/0021999181901455.

Ibrahim, A.M., Padovani, J.I., Howe, R.T., Anis, Y.H., 2021. Modeling of droplet generation in a microfluidic flow-focusing junction for droplet size control. Micromachines 12 (6), URL https://www.mdpi.com/2072-666X/12/6/590.

Kornilovitch, P.E., Cochell, T., Govyadinov, A.N., 2022. Temperature dependence of inertial pumping in microchannels. Phys. Fluids 34 (2), 022003, arXiv:https://doi.org/10.1063/5.0079327.

Kornilovitch, P., Govyadinov, A., Markel, D., Torniainen, E., 2013. One-dimensional model of inertial pumping. Phys. Rev. E 87.

Lake, J., Heyde, K., Ruder, W., 2017. Low-cost feedback-controlled syringe pressure pumps for microfluidics applications. PLoS One 12.

Lotfian, A., Roohi, E., 2019. Radiometric flow in periodically patterned channels: fluid physics and improved configurations. J. Fluid Mech. 860, 544–576.

Ma, T., Sun, S., Li, B., Chu, J., 2019. Piezoelectric peristaltic micropump integrated on a microfluidic chip. Sensors Actuators A 292, 90–96, URL https://www.sciencedirect.com/science/article/pii/S092442471930161X.

Mishchuk, N., Heldal, T., Volden, T., Auerswald, J., Knapp, H., 2009. Micropump based on electroosmosis of the second kind. Electrophoresis 30.

Mutlu, B.R., Edd, J.F., Toner, M., 2018. Oscillatory inertial focusing in infinite microchannels. Proc. Natl. Acad. Sci. 115 (30), 7682–7687, arXiv:https://www.pnas.org/doi/pdf/10.1073/pnas.1721420115, URL https://www.pnas.org/doi/abs/10.1073/pnas.1721420115.

Okuyama, K., Mori, S., Sawa, K., Iida, Y., 2006. Dynamics of boiling succeeding spontaneous nucleation on a rapidly heated small surface. Int. J. Heat Mass Transfer 49 (15), 2771–2780, URL https://www.sciencedirect.com/science/article/pii/S0017931006000238.

Ory, E., Yuan, H., Prosperetti, A., Popinet, S., Zaleski, S., 2000. Growth and collapse of a vapor bubble in a narrow tube. Phys. Fluids 12.

Ruiz, O., 2007. CFD model of the thermal inkjet droplet ejection process. In: ASME/JSME 2007 Thermal Engineering Heat Transfer Summer Conference. In: Heat Transfer Summer Conference, vol. 3, pp. 357–365.

Shizhi, Q., Bau, H., 2009. Magneto-hydrodynamics based microfluidics. Mech. Res. Commun. 36.

Snyder, J., Getpreecharsawas, J., Fang, D., Gaborski, T., Striemer, C., Fauchet, P., Borkholder, D., McGrath, J., 2013. High-performance, low-voltage electroosmotic pumps with molecularly thin silicon nanomembranes. Proc. Natl. Acad. Sci. 110 (46), 18425–18430, arXiv:https://www.pnas.org/content/110/46/18425.full.pdf, URL https://www.pnas.org/content/110/46/18425.

Tan, H., Torniainen, E., Markel, D.P., Browning, R.N.K., 2015. Numerical simulation of droplet ejection of thermal inkjet printheads. Internat. J. Numer. Methods Fluids 77 (9), 544–570, arXiv:https://onlinelibrary.wiley.com/doi/pdf/10.1002/fld.3997, URL https://onlinelibrary.wiley.com/doi/abs/10.1002/fld.3997.

Timoshenko, S., Goodier, J., 1970. Theory of Elasticity, third ed. McGaw-Hill, Inc..

Torniainen, E., Govyadinov, A., Markel, D., Kornilovitch, P., 2012. Bubble-driven inertial micropump. Phys. Fluids 24.

Vinayakumar, K., Nadiger, G., Shetty, V., Dinesh, S., Nayak, M., Rajanna, K., 2017. Packaged peristaltic micropump for controlled drug delivery application. Rev. Sci. Instrum. 88.

Yin, Z., Prosperetti, A., 2005. 'Blinking bubble' micropump with microfabricated heaters. J. Micromech. Microeng. 15.

Yuan, H., Prosperetti, A., 1999. The pumping effect of growing and collapsing bubbles in a tube. J. Micromech. Microeng. 9 (4), 402–413.

Zhou, Y., Ma, Z., Ai, Y., 2018. Sheathless inertial cell focusing and sorting with serial reverse wavy channel structures. Microsyst. Nanoeng. 4 (1), 5.